The INFRA-EAR: a low-cost mobile multidisciplinary measurement platform for monitoring geophysical parameters

Olivier F.C. den Ouden[1,2], Jelle D. Assink[1], Cornelis D. Oudshoorn[3] Dominique Filippi[4] and Läslo G. Evers[1,2]

[1]R&D Department of Seismology and Acoustics, Royal Netherlands Meteorological Institute, De Bilt, The Netherlands
[2]Dept. of Geoscience and Engineering, Delft University of Technology, Delft, The Netherlands
[3]R&D Department of Observations and Data Technology, Royal Netherlands Meteorological Institute, De Bilt, The Netherlands
[4]Sextant Technology Inc., Marton, New-Zealand

Abstract

Geophysical studies and real-time monitoring of natural hazards, such as volcanic eruptions or severe weather events, benefit from the joint analysis of multiple geophysical parameters. However, typical geophysical measurement platforms still provide logging solutions for a single parameter, due to different community standards and the higher cost rate per added sensor.

In this work, the ~~'infrasound-logger'~~ 'Infrasound and Environmental Atmospheric data Recorder' (INFRA-EAR) is presented, which has been designed as a low-cost mobile multidisciplinary measurement platform for geophysical monitoring. The platform monitors in particular infrasound, but concurrently measures barometric pressure, accelerations, wind flow and uses the Global Positioning System (GPS) ~~for positioning of~~ to position the platform. Due to its digital design, the sensor platform can readily be integrated with existing geophysical data infrastructures and be embedded in ~~the analysis of geophysical data~~ geophysical data analysis. The small dimensions and ~~lower~~ low cost price per unit allow for unconventional, experimental designs, for example ~~high density~~ high-density spatial sampling or deployment on moving measurement platforms. Moreover, such deployments can complement existing high-fidelity geophysical sensor networks. The platform is designed using digital Micro-electromechanical Systems (MEMS) sensors ~~that are~~ embedded on a Printed Circuit Board (PCB). The MEMS sensors on the PCB are ~~:~~ a GPS, a three-component accelerometer, a barometric pressure sensor, an anemometer and a differential pressure sensor. A programmable microcontroller unit controls the sampling frequency of the sensors ~~, and the~~ and data storage. A waterproof casing is used to protect the mobile platform against the weather. The casing is created with a stereolithography (SLA) Formlabs 3D printer, using durable resin.

Thanks to ~~a~~ low power consumption (9 Wh over 25 days), the system can be powered by a battery or solar panel. Besides the description of the platform design, we discuss the calibration and performance of the individual sensors.

1 Introduction

Real-time monitoring of natural hazards, such as volcanic eruptions or severe weather events benefit from the joint analysis of multiple geophysical parameters. However, geophysical measurement platforms are typically designed ~~for the measurement of~~ to measure a single parameter, due to different community standards and the higher cost rate per added sensor. The quality and robustness of geophysical measuring equipment generally ~~scales~~ scale with price, due to higher material costs and research and development (R&D) expenses ~~of the manufacturer~~. In addition, the deployment of such equipment comes with complex deployment and calibration procedures ~~,~~ and requires the presence of a robust power and data infrastructure.

Geophysical institutes often place multiple sensor platforms co-located. Meteorological institutes, for example, measure various meteorological parameters for comparison, which improves the weather observations ~~, as well as weather~~ and weather, forecast models. The Comprehensive Nuclear-Test-Ban Treaty Organization (CTBTO) performs various geophysical measurements at its measurement sites where possible. The International Monitoring System (IMS), which is in place for the verification of the CTBT, performs continuous seismic, hydroacoustic, infrasonic and radionuclide measurements [Marty, 2019]. In addition, the IMS infrasound arrays and radionuclide facilities host auxiliary meteorological equipment, as this data facilitates the review of the primary IMS data streams. Besides its use for verifying the CTBT, it has also been shown that a multi-instrumental ~~observation~~ observational network such as the IMS can provide useful information on the vertical dynamic structure of the middle and upper atmosphere, in particular when paired with complementary upper atmospheric remote sensing techniques such as lidar [Blanc et al., 2018]. Other studies that involve the analysis of multiple geophysical parameters include seismo-acoustic analyses of explosions (~~[Assink et al., 2018] [Averbuch et al., 2020]~~[Assink et al., 2018, Averbuch et al., 2020]), earthquakes ([Shani-Kadmiel et al., 2018]), and volcanoes ([Green et al., 2012]).

National Weather Services, such as the Royal Netherlands Meteorological Institute (KNMI), have expressed an interest in measuring weather on a local scale to inform citizens and warn in case of extreme weather. In addition, such measurements allow for higher-resolution measurements of sub-grid scale atmospheric dynamics, which will contribute to the improvement of short-term and now-casting weather forecasts [Manobianco and Short, 2001, Lamr . Therefore it became part of a low-cost citizen weather station program, to increase the spatial resolution of conventional numerical weather prediction models. In the Netherlands, over 300 of those weather stations ~~are contributing~~ contribute to a global citizen science project, Weather Observations Website (WOW)~~[Garcia-Marti et al., 2019] [Cornes et al., 2020]~~[Garcia-Marti et al., 2019, Cornes et al., 2020]. Nonetheless, due to the required infrastructure of the equipment, many platforms are spatially static. Having a low-cost multidisciplinary mobile sensor platform allows for high-resolution spatial sampling and complement existing high-fidelity geophysical sensor networks ~~[Poler et al., 2020]~~(e.g., buoys in the open ocean [Grimmett et al., 2019], and stratospheric balloons [Poler et al., 2020]).

Various disciplines ~~are applying~~ apply new sensor technology to obtain higher spatial and temporal resolution [D'Alessandro et al., 2014] for geophysical hazard monitoring. Micro-electromechanical systems (MEMS) are small single-chip sensors that combine electrical and mechanical components and have ~~a~~ low energy consumption. The seismic community has created low-cost reliable MEMS accelerometers ~~[Homeijer et al., 2011] [Milligan et al., 2011] [Zou et al., 2014]~~[Homeijer et al., 2011, Milligan et al., 2011, Zou et al., 2014] to detect strong accelerations that exceed values due to Earth's gravity field ~~[Speller and Yu, 2004] [Laine and Mougenot, 2007] [Homeijer et al., 2014]~~[Speller and Yu, 2004, Laine and Mougenot, 2007, Homeijer et al., 2014]. Moreover, the infrasound ~~[Marcillo et al., 2012] [Anderson et al., 2018]~~[Marcillo et al., 2012, Anderson et al., 2018], as well as the meteorological community are integrating MEMS sensors into the existing sensor network ~~[Huang et al., 2003] [Fang et al., 2010] [Ma et al., 2011]~~[Huang et al., 2003, Fang et al., 2010, Ma et al., 2011].

In this work, the ~~'infrasound-logger'~~ INFRA-EAR is presented, which has been designed as a low-cost mobile multidisciplinary measurement platform for geophysical monitoring, in particular, infrasound. The platform uses various digital MEMS sensors ~~, which are~~ embedded on a Printed Circuit Board (PCB). A programmable microcontroller unit, as well embedded on the PCB, controls the ~~sampling frequency of the sensors~~ sensors' sampling frequency and establishes the energy supply for the sensors ~~as well as~~ and the data-communication and storage. A waterproof casing ~~protect~~ protects the mobile platform against the weather. The casing is created with a stereo-lithography (SLA) Formlabs 3D printer, using durable resin. Because of ~~it's~~ its low power consumption, the system can be powered by a battery or solar panel.

Previous studies have presented similar mobile infrasound sensor designs [Anderson et al., 2018, Marcillo et al., 2012, RBOOM, which have shown how low-cost, miniature sensors can complement existing measurement network (e.g., volcanic and earthquake monitoring). Those platforms differ from the INFRA-EAR by dimensions, multidisciplinary purpose, and digital design. All sensors of the INFRA-EAR have an in-built ADC, which directly generates digital outputs. Therefore, the INFRA-EAR can be easily integrated into the existing hardware and software sensor infrastructure. Furthermore, the casing design and development is based on the latest technology of 3D printing. Furthermore, the platform design and purpose are adaptive to various monitoring campaigns.

The ability to detect infrasonic signals of interest depends on the ~~strength of the signal~~ signal's strength relative to the noise levels at the receiver side, the signal to noise ratio (SNR). The signal strength depends on the transmission loss that a signal experiences propagating from source to receiver. Infrasound measurements ~~benefits~~ benefit from insights in the atmospheric noise levels (e.g., wind conditions), the meteorological conditions (e.g., barometric pressure, temperature, and humidity), as well as the movement and positioning of the sensors (e.g., accelerations) [Evers, 2008].

While there are clear benefits associated with a MEMS-based mobile platform (e.g., cheap and rapid deployments to (temporarily) increase coverage), MEMS sensors are known to be less accurate than conventional high-fidelity equipment. Especially digital MEMS sensors, which have a ~~build-in~~ built-in Analog-Digital-Converter (ADC), are known for their high self-noise level. Nonetheless, they could be used near ~~a~~ geophysical sources which generate high SNR signals. Several geophysical measurements ~~[Marcillo et al., 2012] [Grangeon and Lesage, 2019] [Laine and Mougenot, 2007] [D'Alessandro et al., 2014]~~ [Marcillo et al., 2012, Grangeon and Le show the benefit of MEMS sensors, and how they complement the existing sensor network.

In this paper, the design and calibration of the ~~'infrasound-logger'~~ INFRA-EAR is discussed. Due to its digital design, the platform can readily be integrated ~~in~~ into existing geophysical sensor infrastructures. The remainder of this article is organized as follows. Section 2 introduces the mobile platform, its design and features. Section 3 describes the various ~~sensor that are~~ sensors embedded on the platform ~~as well as~~ and the relative calibrations with high-fidelity reference equipment. Firstly, a novel miniature digital infrasound sensor is introduced, and its theoretical response is derived. Secondly, the barometric MEMS sensor is discussed. A ~~novel~~ wind sensor which relies on thermo-resistive elements is discussed next, followed by a discussion of the on-board MEMS accelerometer. In Section 4 ~~the~~, the platform's overall performance and design ~~of the platform~~ are discussed and summarized, from which the conclusions are drawn.

2 Mobile platform design

2.1 Circuit design

The mobile platform contains a PCB ~~, which been~~ created to embed the MEMS sensors and ~~to~~ facilitate the electrical circuits. The PCB carries a Digital Low Voltage Range (DLVR) differential pressure sensor, an anemometer, as well as an accelerometer and ~~barometeric~~ barometric pressure sensor, in addition to a GPS for location and timing purposes (Figure ~~7~~1-a). The sensors are controlled by a MSP430 microcontroller, which is integrated on the PCB, and are powered by ~~a~~ an 1800 mAh lithium battery. Protecting the PCB is done with a weather- and waterproof casing, which has been designed (Figure ~~7~~1-b) with the dimensions 110mm x 38mm x 15mm.

The communication between the microcontroller and MEMS sensor on the PCB is either ~~be~~ done by Inter-Integrated Circuit (I2C) or Serial Peripheral Interface (SPI), and depends on the sensor and personal preference. Both communication methods are bus protocols and allow for serial data transfer. However, SPI handles full-duplex communication, simultaneous communication between microcontroller and MEMS sensor, while I2C is half-duplex. Therefore, I2C has the option of clock stretching, and the communication is stopped whenever the MEMS sensor ~~is not able to~~ cannot send data. Besides, I2C has ~~build-in~~ built-in features to verify the data communication (e.g., start/stop ~~bite~~ bit, acknowledgement of data). Although the I2C protocol is favourable, it requires more power. ~~Furthermore, the microcontroller handles the~~

The microcontroller runs on self-made software, complementing the required manufacturers electrical and communication protocols. The software allows determining the sample time, sample frequency, and data

storage. The PCB includes a 64 ~~mb~~ MB flash memory, which is used to store the data. The raw output of the digital MEMS sensors are stored as bits~~.—~~, and the microcontroller performs no data processing to save power consumption. To extract data, the platform needs to be connected to a computer. There are no wireless communication possibilities.

2.2 Casing design for pressure measurements

The mobile sensor platform is designed to measure atmospheric parameters. Hence, a waterproof casing has been created, by a Formlabs SLA 3D printer [Formlabs, 2020], to protect the PCB. Because of the use of a Durable Resin, the casing is waterproof and air-tight. At the bottom of the casing, a dome structure is integrated (Figure 1-c), which acts as an inlet to both the absolute and differential pressure sensors. Note that the dome is not connected to the inside of the casing. The inlets of both sensors and a capillary are integrated ~~in~~ within the dome designs ~~,~~ and sealed with ~~silicon~~ silicone glue, avoiding water and air leakage. Moreover, a Gore-TEX air-vent sticker [Gore-Tex, 2020] is used to cover the dome, which allows airflow but restrains water and salt in case of measurement near or above the ocean.

~~By this design , the volume~~ Air turbulence can generate dynamic pressure effects or stagnation pressure at the pressure dome [Raspet et al., 2019]. The stagnation pressure increases with altitude, which results in higher wind speeds. Atmospheric measurements at altitude might therefore be influenced by stagnation pressure [Bowman and Lees, 2015, Smink et al., 2019, Krishnamoorthy et al., 2020]. The influence of stagnation pressure on pressure measurements is theoretically elucidated by [Raspet et al., 2008].

The application of a quad-disk might remove the stagnation pressure. Quad-disks are developed to cancel dynamic pressure effects, and helps detect slower static pressure changes or acoustic perturbations. Theoretical analysis of the quad-disk indicates that it should remove sufficient dynamic pressure to be useful for turbulence studies [Wyngaard and Kosovic, 1994]. However, recent studies have shown a minimum effect of quad-disks on infrasound recordings [Krishnamoorthy et al., 2020]. The casing of the INFRA-EAR is designed and developed for mobile and rapid deployments at remote places, adding a quad-disk to the design will expand the dimensions of the casing. Moreover, the pressure dome is positioned at the bottom of the casing, not orientated towards the dominant wind direction, in order to minimise the stagnation pressure on the pressure sensors.

Furthermore, within this design the casings volume acts as a backing volume for the differential pressure sensor. One inlet of the differential pressure sensor is attached to the outside (via the dome) while the casing encloses the other inlet. A PEEKsil™ Red series capillary is attached to the outside of the casing, ensuring pressure leakage between the backing volume and the atmosphere.

2.3 GPS

For measuring geophysical parameters on a high-resolution temporal scale, it is crucial to know the position and time of the measurement at high precision. To maintain knowledge regarding the position, a GNS2301 GPS is mounted on the PCB [Texim Europe, 2013]. The GPS has a spatial accuracy of $\pm$ 2.5 m, up to 20km altitude.

Besides providing an accurate position, the GPS also prevents drifting of the ~~internal clock of the microcontroller~~ microcontroller's internal clock under the influence of, for example, weather. The time root mean square jitter, the deviation between GPS and ~~true~~ actual time, is $\pm$ 30 nanoseconds.

3 Sensor descriptions

3.1 Infrasound sensor

The human audible sound spectrum is approximately between 20 to 20,000 Hz. Frequencies below 20 Hz or above 20 kHz are referred to as infrasound and ultrasound, respectively. The movement of large air volumes generates infrasound signals with amplitudes in ~~the range of millipascals~~ millipascals' range to tens

of pascals. Examples of infrasound sources include earthquakes, lightning, meteors, nuclear explosions, interfering oceanic waves and surf [Campus and Christie, 2010]. Detection of infrasound depends on the ~~strength of the signal~~signal's strength relative to the noise levels at a remote sensor (array), i.e., the signal-to-noise ratio. The signal strength depends, in turn, on the transmission loss that a signal experiences, while propagating from source to receiver [Waxler and Assink, 2019]. ~~The noise are predominantly determined by local~~ Local wind noise conditions predominantly determine the noise [Raspet et al., 2019], in addition to the sensor self-noise. Due to the presence of atmospheric waveguides and low absorption at infrasonic frequency [Sutherland and Bass, 2004], infrasonic signals can be detected at long distances from an infrasonic source. Assumed that the source levels are sufficiently high so that the long-range signal is above the ambient noise conditions on the receiver side, and the sensor is sensitive enough to detect the signal.

The infrasonic wavefield is conventionally measured with pressure transducers since such scalar measurements are relatively easy to perform. Those measurements can either be performed by absolute or differential pressure sensors. An absolute pressure sensor consists of a sealed aneroid and a measuring cavity ~~, which is~~ connected to the atmosphere. A pressure difference within the measuring cavity will deflect the aneroid capsule. The mechanical deflection is converted to a voltage [Haak and De Wilde, 1996]. The measurement principle of a differential infrasound ~~sensors~~ sensor relies on the deflection of a compliant diaphragm, which is mounted on a cavity inside the sensor. The membrane deflects due to a pressure difference inside and outside the microphone, which occurs when a sound wave passes. A pressure equalization vent is part of the design to make the microphone insensitive to slowly varying pressure differences originating from ~~long period~~ long-period changes in weather conditions [Ponceau and Bosca, 2010].

Acoustic particle velocity sensors constitute a fundamentally different class of sensors ~~,~~ that measure the airflow over sets of heated wires. This information quantifies the 3-D particle velocity at one location, since the measurement is carried out in three directions ~~[De Bree et al., 2003] [Evers and Haak, 2000]. Although the design of such sensors~~[De Bree et al., 2003, Evers and Haak, 2000]. Although such sensors' design is more involved and the sensors are far more costly, these sensors do allow for the measurement of sound directivity at one position, besides just the loudness.

Various studies show ~~that the~~ sensor self-noise and sensitivity curves of infrasound sensors ~~[Ponceau and Bosca, 2010] [Merchant, 2015] [Slad and Merchant, 2016] [Marty, 2019] [Nief et al., 2019] lie~~[Ponceau and Bosca, 2010, Merchant, 2015, S... . The IMS specifications state that the sensor self-noise should be at least 18 dB below the global low ~~ambient noise curves [Brown et al., 2014], which have been~~ noise curves at 1 Hz [Brown et al., 2014], generated from global infrasound measurements using the IMS. Typical infrasound sensor networks, such as the IMS, ~~make use of analog sensors that are~~ use analogue sensors connected to a separate data logger to convert the measured voltage differences to a digital signal. The ~~characteristic sensitivity of the sensor~~ sensor's characteristic sensitivity determines the sensor resolution, i.e., the smallest difference that ~~can be detected by the sensor~~ the sensor can detect. The resolution of the built-in ~~analog-to-digital~~ analogue-to-digital converters (ADC) and the digitizing voltage range determine the ~~resolution of the datalogger~~datalogger's resolution. Current state-of-the-art ~~dataloggers~~ data loggers have a 24-bit resolution. New infrasound sensor techniques involve digital outputs ~~,~~ since the ADC conversion is realized inside the sensor [Nief et al., 2017, Nief et al., 2019].

3.1.1 Sensor design

In this section, the ~~design of the~~ mobile digital infrasound sensor's design is discussed, the KNMI mini-microbarometer (mini-MB). The design of this instrument is based on the following requirements. The sensor should have a flat, linear, response over a wide infrasonic frequency band, e.g., 0.05 - 10 Hz. The sensor should be sensitive to the range of pressure perturbations ~~that occur~~ in this frequency band, which are in the range of millipascals to tens of pascals. Moreover, the ~~self-noise of both the~~ sensor and logging components' self-noise should be below the ambient noise levels of the IMS [Brown et al., 2014]. Taking this into account, the sensor requires as well to be low-cost (i.e., tens of dollars), small in dimensions (i.e., millimeter), and have a low energy consumption (i.e., milliampere).

In this study, infrasound is measured with a differential pressure sensor. The measurement principle relies on the deflection of a diaphragm, which is mounted between two inlets. One inlet is connected to the atmosphere while the other is connected to a cavity (Figure ~~??~~2). The digital MEMS DLVR-F50D differential pressure sensor from All Sensors Inc [DLVR, 2019] is used as a sensing element within the mini-MB. This sensor has

a ~~dimension of~~ 16.5mm x 13.0mm x 7.3mm dimension and has a linear response between ± 125 Pa with a maximum error band of ±0.7 Pa. A Wheatstone bridge senses the ~~deflection of the diaphragm~~diaphragm's deflection by measuring the changes in the piezo-resistive elements attached to the diaphragm. The ~~output of the sensor~~sensor's output is an analogue voltage, which is ~~an analog voltage, that is~~ subsequently digitized by the built-in 14-bit ADC, offering a maximum resolution of 0.02 Pa/count.

3.1.2 Theoretical response

To measure differential pressure, the atmosphere is sampled through inlet A, which has a low resistance (R_1), and is connected to a small fore-volume (V_1). Inlet B is connected to a backing volume (V_2), which is connected to the atmosphere by capillary that acts as a high acoustic resistance (R_2), which determines the low-frequency cut off. Due to an external pressure wave, an observed pressure difference between the two inlets occurs and causes a deflection of the membrane (C_d) (Figure ~~??~~2-a).

A theoretical response, $D(i\omega)$ for a differential pressure sensor, as function of the angular frequency $\omega(= 2\pi f)$, has been derived by [Mentink and Evers, 2011] following [Burridge, 1971]:

$$D(i\omega) = \frac{i\omega\tau_2}{1 + i\omega\tau_2 A + (i\omega)^2 \tau_1 \tau_2 B} \tag{1}$$

where,

$$A = 1 + \frac{\tau_1}{\tau_2} + \frac{R_1}{R_2} + \frac{C_d}{C_2}, \quad B = 1 + C_d(\frac{1}{C_1} + \frac{1}{C_2}) \tag{2}$$

$$\tau_j = R_j C_j, \quad C_j = \frac{V_j}{P_{\text{atm}}\gamma} \tag{3}$$

and P_{atm} indicates the ambient barometric pressure, and γ is the thermal conduction of air. τ_j represent the time constants, and depend on R_1, and R_2, which are the resistances of the inlet and capillary, and C_1, and C_2, the capacities of the fore and backing volume.

KNMI mini-MB sensor specifications			
Components		**Conditions**	
Inlet length	$l_1 = 3\text{x}10^{-2}\text{m}$	Ambient pressure	$P_{\text{atm}} = 101\text{x}10^3\text{Pa}$
Inlet diameter	$a_1 = 2\text{x}10^{-2}\text{m}$	Isothermal gas constant	$\gamma_{iso} = 1$
Capillary length	$l_2 = 5\text{x}10^{-2}\text{m}$	Adiabatic gas constant	$\gamma_{adi} = 1.403$
Capillary diameter	$a_2 = 1\text{x}10^{-4}\text{m}$	Thermal conductivity	$\kappa = 2.5\text{x}10^{-2}\text{ W m}^{-1}\text{ K}^{-1}$
Diaphragm sensitivity	$C_d = 7.5\text{x}10^{-11}\text{m}^4\text{s}^2\text{kg}^{-1}$	Heat capacity	$\rho\,c_p = 1.1\text{x}10^3\text{ J m}^{-3}\text{ K}^{-1}$
Parameters			
Inlet resistance	$R_1 = 8.7\text{x}10^3\text{ kg m}^{-4}\text{ s}^{-1}$	Fore volume	$V_1 = 4.5\text{x}10^{-7}\text{ m}^3$
Capillary resistance	$R_2 = 2.3\text{x}10^{10}\text{ kg m}^{-4}\text{ s}^{-1}$	Backing volume	$V_2 = 16.5\text{x}10^{-6}\text{ m}^3$
Size fore volume	$L_1 = 2\text{x}10^{-4}\text{m}$	Size backing volume	$L_2 = 4\text{x}10^{-4}\text{m}$

Table 1: KNMI mini-MB components, parameter values and standard conditions used in the computations.

Figure ~~??~~2-a represents the sensor setup from an acoustical perspective, where Figure ~~??~~2-b represents the electrical ~~analogs~~ analogues of the sensor. The acoustical pressure difference ($p' = p'_1 - p'_2$) and volume flux (f') are interpreted as an electrical voltage ($U = U_1 - U_2$) and current (I). The equivalent of the electrical resistance (R) corresponds to the ratio between acoustical pressure and the volume flux, whereas the capacitance (C) relates to the ratio of volume and ambient barometric pressure. The ~~mechanical sensitivity of the diaphragm~~ diaphragm's mechanical sensitivity (C_d) is the ratio of volume change and pressure change [Zirpel et al., 1978].

From an analysis of Eq. 1, it follows that inlet A dominates in the high-frequency limit. Hence, $1/2\pi\tau_1$ indicates the high-frequency cut-off of the sensor:

$$\lim_{\omega \to +\infty} D(i\omega) \sim \frac{1}{i\omega\tau_1 B} = \frac{1}{\frac{i\omega R_1 V_1}{P_{\text{atm}}}\left(1 + C_d\left(\frac{P_{\text{atm}}}{V_1} + \frac{P_{\text{atm}}}{V_2}\right)\right)} \tag{4}$$

While at low frequencies it is obtained that frequencies much smaller than $1/\tau_2$ are averaged out. Therefore the low-frequency limit can be determined as:

$$\lim_{\omega \to 0} D(i\omega) \sim i\omega = \frac{i\omega R_2 V_2}{P_{\text{atm}}} \tag{5}$$

which is controlled by the characteristics of the capillary, R_2, and the size of the backing volume, V_2. The acoustical resistance of the inlet R_1 and the capillary R_2 is described by using Poiseuille's law [Washburn, 1921], which couples the resistance of airflow through a pipe (i.e., an inlet or capillary) to its length l_j and diameter a_j, by:

$$R_j = \frac{8 l_j \eta}{\pi a_j^4} \tag{6}$$

Where η stands for the viscosity of air, which equals 18.27 μPa·s at 18°C. Combining Equations 5 and 6 results in the theoretical low-frequency cut-off:

$$f_l \sim \frac{P_{\text{atm}}}{2\pi R_2 V_2} \tag{7}$$

Besides the high and low ends of the response, it is of interest to determine the sensor response behavior within the passband $((\tau_2^{-1} < \omega < \tau_1^{-1}))$.

$$D(i\omega) \sim (\tau_2^{-1} < \omega < \tau_1^{-1}) = \frac{1}{1 + \underbrace{\tau_1/\tau_2}_{1} + \underbrace{R_1/R_2}_{2} + \underbrace{C_d/C_2}_{3}} \tag{8}$$

The three contributions in the denominator influence the passband ~~behavior~~ behaviour of the sensor:

1. A broadband frequency response depends on a constant pressure within the reference volume over the frequencies of interest (i.e., $\tau_1 \ll \tau_2$)

2. The pressure difference at the diaphragm is determined by the relative acoustical resistances ~~that are~~ connected to the sensor. The stability of the sensor response is assured by the ~~large resistance of the capillary~~capillary's large resistance, because of which $R_1 \ll R_2$.

3. The sensor response depends on the ratio between the volumetric displacement of the diaphragm (C_d) versus the reference volume (C_2). For the mini-MB, this term can be neglected.

Figure ~~1~~3 shows the theoretical sensor frequency response for amplitude (Fig. ~~1~~3-a) and phase (Fig. ~~1~~3-b) for isothermal (red) and adiabatic (blue) behavior. The transitional ~~behavior~~ behaviour of the sensor response between isothermal and adiabatic ~~behavior~~ behaviour will be discussed in the next section.

3.1.3 Adiabatic-Isothermal transition

Due to the presence of heat conduction within the sensor, ~~the compressive behavior of air~~air's compressive behaviour is neither isothermal nor adiabatic. Instead, a transition from isothermal to adiabatic ~~behavior~~ behaviour is expected in the infrasonic frequency band ~~[Richiardone, 1993] [Mentink and Evers, 2011]~~[Richiardone, 1993, Men . In the transition zone, the heat capacity ratio can be effectively described by:

$$\overline{\gamma} = \Lambda \gamma \tag{9}$$

where Λ indicates the correction factor, to heat capacity ratio γ. A difference in Λ will influence the capacitance values of the fore and backing volumes (Eq. 3).

Whether a sound wave in an ~~enclusure~~ enclosure behaves isothermally or adiabatically depends on the size of the thermal penetration depth δ_t relative to characteristic length L of the enclosure. L is defined as the ratio between the enclosure's volume and surface ~~of the enclosure~~, i.e. $L = \frac{V}{S}$. The thermal penetration depth is specified as the gas layer thickness in which heat can diffuse through, during the time of one wave period and is derived as $\delta_t = \sqrt{\frac{2\alpha}{\omega}}$. Where $\alpha = \frac{\kappa}{\rho c_p}$ indicates the thermal diffusivity, defined as ratio of thermal conductivity (κ) and heat capacity per unit volume (ρc_p). Adiabatic gas behaviour is obtained when $\frac{\delta_t}{L} \ll 1$, isothermal gas behaviour when $\frac{\delta_t}{L} \gg 1$. The correction factor Λ is a function of δ_t/L, and is thus ~~frequency dependent~~ frequency-dependent, which can be derived as:

$$|\Lambda| = \sqrt{X^2 + Y^2}, \quad \arg(\Lambda) = \frac{\pi}{2} + \arctan(\frac{X}{Y}) \tag{10}$$

where

$$X = x(\gamma_{adi} - 1) - \gamma_{adi}, \quad Y = y(\gamma_{adi} - 1) \tag{11}$$

x and y represent the real and imaginary components of a complex-valued function $Z(\frac{\delta_t}{L})$, which is dependent on the geometrical shape of the enclosure and the thermal pentration depth. In between the adiabatic and isothermal limits, the correction factor Λ describes the transition from an adiabatic heat ratio (i.e., $\gamma = 1.4$) to an isothermal heat ratio, i.e. $\gamma = 1$. The transition frequency $\bar{f}$ defines the point where the maximum correction of Λ occurs, i.e., for which $L\delta_t \approx 1$, from which follows that ~~$\bar{f} = \frac{\alpha}{\pi L^2}$~~ $\bar{f} = \frac{\alpha}{\pi L^2}$.

In the case of the mini-MB, the fore and backing volume have different shapes and sizes. The backing volume can be described as a long cylinder, L_2, whereas the fore volume has ~~the shape of a rectangular~~ a rectangular shape, L_1. According to those geometries, the transition frequency $\bar{f}$ of the fore and backing volume are 0.5 and 2.2 Hz, respectively. Since $\overline{f}_1 \cdot \tau_1 \ll 1$ and $\overline{f}_2 \cdot \tau_2 \gg 1$ the sensor response above τ_1^{-1} is adiabatic, while the response below τ_2^{-1} is isothermal. Therefore ~~the main effect of the~~, the thermal conduction correction's main effect is found to be in the passband region (Eq. 8).

The mini-MB has been designed to have a broadband response, therefore only the third term of the dominator is influenced by the correction factor. The effect of thermal conduction to the response is due to ratio $\frac{C_d}{C_2}$, which means that the correction factor is characterized by the geometric component of the backing volume.

$$Z(\frac{\delta_t}{L}) = 1 - \frac{2J_1(\zeta)}{\zeta J_0(\zeta)} \tag{12}$$

here Z indicates the characteristic correction assuming a long cylinder [Mentink and Evers, 2011]. $\zeta = \sqrt{-2i}\frac{L}{\delta_t}$ indicates the ratio of L to δ_t, while J_0 and J_1 are zeroth and first order Bessel functions of the first kind.

The corrected theoretical sensor response is obtained by substituting $\overline{C_j} = \frac{C_j}{\Lambda}$. Figure ~~1~~3-c shows the value of $\overline{\gamma}$ in the transaction zone between isothermal and adiabatic gas behaviour. The black line in Figure ~~1~~3-a and b indicates the corrected theoretical sensor response.

In the case of the mini-MB the isothermal-to-adiabatic transition results in an effect on the amplitude of $\Delta|D| = (\gamma - 1)\frac{C_d}{C_2} = 2.8\%$ and on the phase of less than a degree. Note that $\frac{C_d}{C_2} \ll 1$ implies that the backing volume is relatively large such that the change in gas ~~behavior~~ behaviour does not influence the sensitivity of the diaphragm.

3.1.4 Gore-Tex air-vent

As discussed in Section 3.1.2., the high and low-frequency cut-off are controlled by the resistivity of the inlet and backing volume, respectively. A Gore-Tex V9 sticker is added to the opening of the ~~pressure dome of the casing~~ casing's pressure dome, which changes the resistivity of the inlets. The Gore-Tex V9 vent allows

318 an airflow of $2\mathrm{x}10^{-8}\mathrm{m}^3\mathrm{s}^{-1}\mathrm{m}^{-2}$. Poiseuille's second law, Equation 6, shows the airflow resistivity caused by
319 an open pipe, and can be re-written as;

$$R_j = \frac{\Delta p}{q_v} \tag{13}$$

320 where Δp indicates the pressure difference between both sides of the pipe, and q_v the volumetric airflow.

321 For the differential pressures that the mini-MB sensor is able to sense, ranging from 0.02 to 125 Pa,
322 with a Gore-Tex air-vent area of $5\mathrm{x}10^{-2}$ m^2, the equivalent resistivity R_{gore} is ranging from $5\mathrm{x}10^5$ to
323 $3.125\mathrm{x}10^8\mathrm{kgm}^{-4}\mathrm{s}^{-1}$. Comparing the resistivity of the air-vent with the resistivity values of the capillary
324 and the ~~sensors inlet~~ inlet of the sensor, Table 1 ~~, it follows that only the resistivity of the inlet will be~~
325 ~~influenced by the air-vent~~shows that the air-vent will only influence the inlet's resistivity. Assuming the vent
326 behaves linear, the ~~high frequency~~ high-frequency cut-off of the sensor decreases to a value of around 15 Hz.
327 Figure ~~1~~ 3 shows the theoretical transfer function for the mini-MB with a Gore-Tex air-vent attached to the
328 inlet. The ~~high frequency~~ high-frequency cut-off is shifting between the dotted line and the dashed line, due
329 to varying values of R_{gore}.

3.1.5 Experimental response

331 The theoretical sensor response describes the high and low-frequency cut-off. ~~From~~ Eq. 7 and the parameters
332 listed in Table 1 ~~, it follows~~ show that the mini-MB has a theoretical low-frequency cut-off of 0.042Hz. A
333 sudden over or under pressure (i.e., impulse response) is applied to the sensor to determine the low-frequency
334 cut-off experimentally[Evers and Haak, 2000]. The impulse forces the diaphragm out of equilibrium. The
335 capillary and the size of the backing volume control the time to return into equilibrium again. The time it
336 takes for the diaphragm to reach equilibrium again corresponds to a characteristic relaxation time ~~that is~~
337 proportional to the low-frequency cut-off.

338 The outcome of the experimental low-frequency cut-off was determined to be 0.044±0.0025Hz. The theoretical
339 ~~low frequency~~ low-frequency cut-off falls within the error margins of the experimental cut-off frequency. ~~Small~~
340 The small difference between both ~~are~~ is assumed to be due to experimental errors in timing the relaxation
341 time as well as small imperfections in the used capillary [Evers, 2008]. It follows from Eq. 6 that the low-
342 frequency cut-off is inversely proportional to the radius to the fourth power. Hence, a one ~~percent~~ per cent
343 deviation in the capillary radius will lead to a four ~~percent~~ per cent deviation in low-frequency cut-off.

3.1.6 Sensor self-noise

345 The resolution, the smallest change detectable by a sensor, depends on the sensor measurement range and
346 the number of ADC bits. Having a linear response over a pressure range of ± 125 Pa and a 14-bit ~~build-in~~
347 built-in, ADC results in a ~~resolution of~~ 0.02 Pa/count resolution. The accuracy of the measurement depends,
348 besides the ADC resolution, on the ~~internal error of the sensor~~sensor's internal error, the self-noise. The
349 self-noise corresponds to the ~~deformation of the diaphragm~~diaphragm's deformation caused by the mass of
350 the diaphragm plus the electrical noise from the digitiser. As it is a digital sensor, it is ~~not possible~~ impossible
351 to follow the conventional methods to determine self-noise [Sleeman et al., 2006]. Therefore the self-noise is
352 determined by opening both inlets to a closed pressure chamber, ensuring no pressure difference between
353 ~~both inlets~~them. The outcome stated that the self-noise falls within the sensor's maximum error band~~of~~
354 ~~the sensor~~, ±0.7 Pa [DLVR, 2019]. Since no backing volume is used, and the cavities at both sides of the
355 diaphragm are small, the relation $\frac{C_d}{C_2}$ changes (Eq. 8). Due to this, it is necessary to correct the sensor
356 response for the adiabatic to isothermal transition. (Section 3.1.3).

357 The ~~consistency of the~~ self-noise consistency is determined by calculating the Power Spectral Density (PSD)
358 curves for each hour over a test period of 24 hours [Merchant and Hart, 2011]. Figure ~~2~~4-a shows in black
359 the average 90 percentile confidence interval of the self-noise. Note that the instrumental self-noise exceeds
360 the global low noise model [Brown et al., 2014] at frequencies above 0.4 Hz. Compared to high-fidelity
361 equipment that typically ~~fall completely~~ falls entirely below the global low noise models, such self-noise levels
362 are relatively high, yet comparable to levels ~~that are~~ attained by similar sensor designs [Marcillo et al., 2012].

363 Furthermore, note that the self-noise follows the dynamic range of a 12-bit ADC, as indicated by the gray
364 dotted line [Sleeman et al., 2006]. The sensor has a maximum 'no missing code' of 12-bits, the effective
365 number of bits [DLVR, 2019].

3.1.7 Sensor comparison

367 A comparison between the mini-MB and a Hyperion IFS-5111 sensor [Merchant, 2015] is made to assess the
368 ~~performance of the~~ mini-MB performance relative to the reference Hyperion sensor. Both sensors have been
369 placed inside a cabin next to the outside sensor test facility at the leading author's institute. There is a con-
370 nection to the outside pressure field through air holes in the wall of the cabin. The Hyperion sensor has been
371 configured with a high-frequency ~~(HF)~~ shroud. Figure ~~2~~4-a and b show the PDF [Merchant and Hart, 2011]
372 of the data recorded by the mini-MB and the Hyperion sensor, respectively. Both sensors resolved the char-
373 acteristic microbarom peak around 0.2Hz [Christie and Campus, 2010]. The spectral peaks above 10 Hz
374 correspond to resonances that exist inside the measurement shelter.

375 A direct comparison of the pressure recordings ~~is~~ are shown in Figures ~~2~~4-c, -d, and -e. Figure 2-c shows the
376 absolute difference in amplitude over frequency, where panel d indicates the phase difference between both
377 sensors. Panel e shows the relative difference between the mini-MB and the Hyperion sensor. The sensors
378 are in good agreement over the passband frequencies. A larger deviation is shown for the low end ($f < 0.07$
379 Hz) and high end frequencies($f > 8$ Hz). At frequencies between 0.07 and 1 Hz, the pressure values are
380 positively biased by 5 ± 1 dB, which equals ~~an error~~ a measurement error by the KNMI mini-MB of $\pm$ 0.005
381 Pa (Figure ~~2~~4-e). Above 1 Hz, the pressure values are biased by 10 ± 5 dB, which equals ~~an~~ a measurement
382 error of $\pm$ 0.02 Pa.

383 The backing volume causes a deviation in the ~~low frequency spectrumis caused by the backing volume. The~~
384 ~~high frequency~~ low-frequency spectrum. The high-frequency deviation is due to the relatively high noise level
385 of the mini-MB. For the higher frequencies, the mini-MB PDF follows the 12-bit dynamic range. Only in case
386 of significant events or loud ambient noise, the sensor ~~is capable of sensing~~ can sense pressure perturbations
387 in the high-frequency range. Nonetheless, ~~over the entire frequency band the~~ the mini-MB falls within a 30
388 dB error range over the entire frequency band compared to the Hyperion IFS-5111 sensor.

3.2 Meteorological parameters

390 The detectability of infrasound is directly linked to wind noise conditions and the ~~stability of the atmospherein~~
391 ~~the surrounding of the infrasound sensor,~~ atmosphere's stability in the infrasound sensor's surrounding since
392 noise levels are increased when turbulence levels are high. Therefore, it is beneficial to have simultaneous
393 measurements of the basic meteorological parameters, i.e., pressure, wind and temperature. The sub-sections
394 below describe the different meteorological measurements contained on the sensor platform.

3.2.1 Barometric pressure sensor

396 The barometric pressure is sensed by the LPS33HW sensor [STMicroelectronics, 2017], which is part of the
397 pressure dome. Similarly to the differential pressure sensor, piezo-resistive crystals measure the barometric
398 pressure.

399 Calibration tests are performed within a pressure chamber, in which a cycle of static pressures between 960
400 and 1070 hPa can be produced. Besides the MEMS sensor, the chamber is equipped with a reference sensor.
401 This procedure resulted in a calibration curve, which describes the ~~pressure dependent~~ pressure-dependent
402 systematic bias. After correcting for the bias, the LPS sensor has an accuracy of $\pm$ 0.1 hPa, i.e., the LPS
403 sensors measures values ~~that are~~ within $\pm$ 0.1 hPa of the value measured by the KNMI reference sensor.
404 Furthermore, the LPS sensor has been ~~field tested, along~~ field-tested (Figure 5-a), along with a Paroscientific
405 Digiquartz 1015A barometer, which has an accuracy of 0.05 hPa. From the distribution of observations, it
406 can be estimated that the LPS sensor has a precision of $\pm$0.1 hPa for 93% of the time (Figure 5-b). For the
407 remainder, the maximum deviation was $\pm$0.15 hPa.

3.2.2 Wind sensor

The pressure field at infrasonic frequencies consists, in addition to coherent acoustic signals, to a large degree of pressure perturbations due to wind and turbulence ~~, and which is generally referred to as wind-noise [Walker and Hedlin, 2010]. Wind noise~~ [Walker and Hedlin, 2010]. This turbulent energy is present over the complete infrasonic frequency range with a typical noise amplitude level decrease with increasing frequencies, following a $f^{-5/3}$ slope [Raspet et al., 2019].

~~For the reduction of wind noise~~ To reduce wind turbulence interference with the acoustic perturbations, a Wind-Noise-Reduction-System (WNRS) can be put in place ~~[Walker and Hedlin, 2010] [Raspet et al., 2019]~~ [Walker and Hedlin, 2010, Raspet et al., 2019]. Most WNRSs ~~applied~~ consist of a non-porous pipe rosette, with low impedance inlets at ~~the end of each pipe~~ each pipe's end. All pipes are connected to four main pipes, which connect to the microbarometer. Doing so, the atmosphere is sampled over a larger area, and thus small incoherent pressure perturbations (e.g., wind) are filtered out.

The sensor presented in this paper is designed for mobile sampling campaigns. In such cases, the application of similar WNRS filters cannot be attained. Not having a WNRS decreases the SNR, measuring wind with an anemometer will give an insight into the wind conditions. Therefore, a simultaneous measurement of wind and infrasound provides better insight into the infrasonic SNR conditions.

Sensor design

~~To measure the wind conditions, a~~ A 2D ~~omni-directional~~ omnidirectional heat mass flow sensor has been designed to measure the wind conditions, which is a robust and passive anemometer (Figure ~~3~~6-a). The sensor is built with a central heating element, which heats ~~up~~ to approximately 80°C, and is circularly surrounded by six TDK thermistors [TDK, 2018]. Depending on the wind direction and speed, the temperature field around the center element is modified. The wind speed and direction can be estimated from the 2D temperature gradient, i.e., its absolute value and direction.

Theoretical response

The six sensing elements are placed within a distance of one centimeter from the heating element, while two thermistors and the heating element are at a spatial angle of 60°. The thermistors ~~are used to~~ measure the temperature gradient ~~that is~~ caused by the wind flow ~~,~~ since the resistance is strongly sensitive to temperature. The thermistors are made of semiconductor material and have a negative temperature coefficient. The resistance decreases non-linearly with increasing temperature. The Steinhart-Hart equation approximately describes the temperature T as a function of resistance value R_Ω [Steinhart and Hart, 1968]:

$$\frac{1}{T} = C_{\Omega_1} + C_{\Omega_2}(\ln(R_\Omega)) + C_{\Omega_3}(\ln(R_\Omega)^3) \tag{14}$$

where ~~$C_{\Omega_1}, C_{\Omega_2}$, and C_{Ω_3}~~ $C_{\Omega_1}, C_{\Omega_2}$, and C_{Ω_3} are the thermistor constants ~~, which can~~ received by the manufacturer [TDK, 2018]. However, they can as well be determined by taking three calibration measurements, for which the temperature and resistance are known, and solving the three equations simultaneously. Figure ~~3~~6-b shows the sensitivity curve for the TDK thermistor. The thermistor has a relative value of 1Ω at $25°C$, and a precision of $\pm 4\%/°C$, which leads to a 0.05°C error. ~~In the next section, this~~ This error value is placed in context by modeling the expected temperate difference under representative meteorological conditions in the next section.

Numerical sensor response

The heating element needs to ~~be able to~~ transfer a minimum temperature difference around the sensing elements (i.e., the sensing elements error). A numerical model has been built in ANSYS [ANSYS,] to define the amount of temperature difference around the sensing elements under different meteorological circumstances. The model is a first approximation of the sensitivity and is based on homogeneous laminar

450 airflow passing by the sensor. Turbulent flow, along the anemometer~~causes uncertainties in wind direction~~
451 ~~and speed~~, caused by the sensor design or casing, generates uncertainties within the measurements.

452 This ~~approach~~ first approximation of sensitivity follows a numerical forward modeling technique to approxi-
453 mate the ~~shape of the heat probe~~~~and its~~ heat probe's shape and intensity at a sensing element. The model
454 was run at stable meteorological parameters (i.e., 8°C air temperature, 50% humidity, and 10 m/s wind
455 speed). The outcome shows that under those circumstances, the sensing element experiences a temperature
456 difference of around 4°C. Together with the outcome of the ~~sensitivity curve of the thermistors~~thermistors'
457 sensitivity curve, it is concluded that the designed sensor can resolve this airflow and is used to estimate
458 wind speed and direction.

Conversion of sensor output into atmospheric parameters

460 To convert the measured resistivity into atmospheric parameters, a 2D planar temperature gradient has
461 been estimated numerically from the discrete set of measurements. The measurement resistivities have been
462 transformed into temperature measurements following Eq. 14. Based on those temperatures, a 2D numerical
463 temperature gradient has been reconstructed. The problem is analogous to the estimation of the wave-front
464 directivity from travel time differences [Szuberla and Olson, 2004].

465 In the present case, there are $N = 6$ discrete sample points, each with an $r_j = (x_j, y_j)$ coordinate and a
466 temperature value T_j. The total differential of the temperature describes the variation of temperature $T(x, y)$
467 as a function of x and y:

$$dT = \frac{\partial T}{\partial x}dx + \frac{\partial T}{\partial y}dy. \tag{15}$$

468 From equation 15, it follows that we can determine the two dimensional gradient $\nabla T = (\frac{\partial T}{\partial x}, \frac{\partial T}{\partial y})$ by setting
469 up a system of N equations. In this case, the number of unknowns is two, and thus the gradient could be
470 estimated by two measurements. However, in practice, errors are introduced due to measurement errors.
471 Therefore the set of equations becomes inconsistent, which leads to nonsensical solutions. The unknown set
472 of parameters is solved by over-determining the system in a least-squares sense to overcome this problem.
473 Equation 15 can be rewritten in terms of a matrix-vector system:

$$\mathbf{y} = \mathbb{X}\mathbf{p} + \epsilon \tag{16}$$

474 where $\mathbf{y}$ represents the temperature difference between two measurement points, matrix $\mathbb{X}$ represents the
475 $M = \frac{N(N-1)}{2}$ pair-wise separations and $\mathbf{p}$ represents the temperature gradient ∇T. It is assumed that the
476 measurement errors ϵ can be described by a normal distribution, i.e. a random variable with mean $E(\epsilon) = 0$
477 and variance $Var(\epsilon) = \sigma^2$. It can be been shown that the least-squares estimate of $\mathbf{p}$, here labeled $\hat{\mathbf{p}}$, can be
478 obtained by solving the following equation:

$$\hat{\mathbf{p}} = (\mathbb{X}^{\dagger}\mathbb{X})^{-1}\mathbb{X}^{\dagger}\mathbf{y} \tag{17}$$

$$\mathbf{p_x} = \frac{\hat{\mathbf{p}}_x}{\hat{\mathbf{p}}_x^2 + \hat{\mathbf{p}}_\mathbf{y}^2}, \qquad \mathbf{p_y} = \frac{\hat{\mathbf{p}}_y}{\hat{\mathbf{p}}_x^2 + \hat{\mathbf{p}}_\mathbf{y}^2} \tag{18}$$

479 where † represents the transpose operator, the solution satisfies equation 16 with the constraint that the sum
480 of squared errors is minimized. The matrix $\mathbb{X}$ and the error term ϵ determine the solution's accuracy. If a
481 Gaussian distribution can represent the measurement errors, it can be shown that the least-squares solution
482 is unbiased.

483 Bases on the 2D reconstruction of the temperature gradient (Equation 18), the wind direction and speed is
484 resolved, with an estimated accuracy. Furthermore, this method allows determining the uncertainty based
485 on geometric sensor set-up [Szuberla and Olson, 2004]. Figure 6-c shows the least-squares error analyses of

the sensor design (Figure 6-a). It stands out that the uncertainty increases when one element is positioned close to the wind flow (i.e., at 60°).

Reference calibration

Experimental calibration of the anemometer has been performed at the KNMI's calibration lab. The calibration lab features a wind tunnel, which generates a laminar airflow ranging between 0 - 20 m/s. Within the wind-tunnel, two mechanical anemometers are installed, which serve as reference sensors. ~~The mobile platform with~~ With its MEMS anemometer, the mobile platform is installed right below one of the reference sensors to ensure that the mobile platform does not obstruct the laminar flow in the tunnel.

The calibration procedure consists of multiple independent calibration tests that will be described next. First, the sensor is placed inside the wind tunnel while there is no airflow. This way, the relative difference between the sensing elements is determined, the so-called zero-measurement. ~~By correcting for the relative difference, the~~ The sensor is corrected for the internal bias by correcting for the relative difference, which varies around $\pm$ 25 ohm. After correcting ~~for~~ the sensor bias, the sensor is placed within the horizontal plane (i.e., with a pitch angle of 0°) at different angles ~~with respect to the air flow~~ concerning the airflow. For every angle, the flow speed is varied between 0 ~~tot~~ to 20 m/s.

The calibration shows that the measured resistance of the thermistors increases with increasing wind speeds. High wind speeds increasingly cool down the thermistors, resulting in higher resistances. Figure ~~3-c shows the measured resistance of the six thermistors over the~~ 6-d shows the six thermistors' measured resistance over the actual wind speed. ~~To convert resistance into wind speed, a polynomial curve has been fitted over the average measured resistance (Fig. 3-c, black line).~~

The ~~accuracy of the wind direction is determined by interpolating the measured velocities into a gradient field over the sensor. The wind direction is obtained by calculating the mean gradient vector of this gradient field.~~ wind direction and the accuracy of the anemometers have been determined according to Eq. 17. Three different sensor set-ups show the accuracy and precision over increasing wind speeds as a function of directivity. The outcome of calibration set-ups 1 (270°), 2 (90°), and 3 (60°) are shown respectively in Figure ~~3-d, 6~~-e, ~~and~~ -f. The mean direction over all wind speeds, for the three set-ups, ~~are 93°, 265°, and 62°~~ is 89°, 272°, and 57°. The standard deviation shows that the ~~accuracy of the sensor is ±18°~~ sensor's accuracy is ±5°. Furthermore, it is shown that the precision of the wind direction increases with increasing wind speeds.

The resolved wind speeds by the anemometer and the difference with the correct wind speed are shown in Figure 6-e. The colors indicate the difference between resolved wind speed and correct wind speed within the wind tunnel. The mean deviation between resolved and correct wind speed is ±2 m/s. Again, it is shown that the accuracy increases with increasing wind speeds.

3.3 Accelerometer

The sensing element of the infrasound sensor on this platform is a sensitive diaphragm. Strong accelerations of the platform will cause a deflection of the diaphragm and may obscure infrasonic signal levels. In addition, such accelerations may be ~~interpreted erroneously~~ misinterpreted as infrasound if no independent accelerometer information is available. To be able to separate the mechanical response of the sensor from actual signals of interest, the platform measures accelerations for which the LSM303, a 6-axis inertial measurement unit (IMU), is deployed [STMicroelectronics, 2018]. The LSM303 consists of a 3-axis accelerometer and 3-axis magnetometer. The measurement range of the accelerometer varies between approximately 2-16 g. The magnetometer is out of the scope of this study ~~,~~ and therefore neglected for the remainder.

Accelerometers measure differential movement between the gravitational field vector and its reference frame. In the absence of linear acceleration, the sensor measures the rotated gravitational field vector, which can be used to calibrate the sensor. A rotational movement of the sensor will result in ~~an~~ acceleration. The IMU is a digital sensor with a built-in 16-bits ADC and has a resolution of 0.06 mg when choosing the lowest measurement range.

A comparison test has been carried out in the seismic pavilion of the author's institute. Inside this pavilion, the LSM is compared to a Streckeisen STS-2 seismometer connected to a Quanterra Q330, as a reference

sensor [KNMI, 1993]. Both sensors are installed on pillars, to ensure a good coupling between the subsurface and the sensor. The comparison test, which is based on 24 hours of recording, shows that the accuracy of the LSM303 3-axis accelerometer is ± 1.5 mg (1.5 cm/s^2). Figure 7 shows the PDF's of the comparison test for the MEMS and STS-2 sensor. While the sensors are deployed on the same seismic pillar and are thus subject to similar seismic noise conditions, the MEMS sensor could not measure ambient seismic noise ([Peterson, 1993, McNamara and Buland, 2004]) due to its high self-noise level. The LSM accelerometer exceeds both the U.S. Geological Survey New High Noise Model (NHNM) [Peterson, 1993] and the STS-2 reference sensor by at least 35 dB.

It is therefore unlikely to use this IMU for monitoring purposes of ambient seismic noise or teleseismic events. Previous studies drew similar conclusions concerning the performance of MEMS accelerometers. Various calibration set-ups are considered while comparing MEMS accelerometers with conventional accelerometers of geophones [Hons et al., 2008, Albarbar et al., 2009, Anthony, each concluding that the accuracy of the MEMS is not sufficient for recording ambient seismic noise. However, strong local events or boisterous environments the MEMS sensor will resolve those seismic signals.

4   Discussion and Conclusion

In this study, the constructional efforts and calibration protocols of the INFRA-EAR are presented. The INFRA-EAR is a low-cost mobile multidisciplinary sensor platform for the monitoring of geophysical quantities. It includes sensors for the measurement of infrasound, acceleration, as well as barometric pressure and wind.

The platform uses the newest sensor technology, i.e., digital MEMS, which have a built-in ADC. The MSP430 programable microcontroller unit controls the sampling of the ADC and the storage of the data samples. A MEMS GPS is a unit to determine the positioning and to prevent clock-drift. Due to the small dimension of MEMS, and their low energy consumption, the "infrasound-logger" is a pocket-size measurement platform, powered by an 1800 mAh lithium battery. The platform does not require any infrastructure (e.g., data connection, power supply and specific mounting) like commonly used for the deployment of high-fidelity systems, which makes it mobile and allows rapid deployments and measurements at remote places.

The INFRA-EAR is specifically designed to measure infrasound. The platform hosts the KNMI mini-MB, a novel design with a pressure dome as inlet, the casing as backing-volume with a PEEKsil capillary, and the DLVR-F50D as sensing element. The low-frequency cut-off of mini-MB depends on the size of the backing volume, and the capillary characteristics. The high-frequency cut-off depends on the mini-MB inlet parameters, which is partly controlled by a Gore-Tex air-vent (Section 3.1.4). The "infrasound-logger" has a low-frequency cut-off frequency of 0.044 ± 0.0025 Hz, while the high-frequency cut-off varies between 15 and 90 Hz.

A comparison between the mini-MB and a Hyperion infrasound sensor [Merchant, 2015] have shown the differences in amplitude and phase (Figure 4). The mini-MB has an amplitude difference of 30 dB for the passband frequencies band compared to the Hyperion sensor. The sensors are in good agreement for the lower frequencies, and both sensors resolved the characteristic microbarom peak around 0.2 Hz [Christie and Campus, 2010]. However, the higher frequencies show small deviations, which is due to the relatively high noise band of the mini-MB. From 8 Hz onward, the mini-MB PDF follows the 12-bit dynamic range of the ADC. Nonetheless, the mini-MB can resolve the infrasonic ambient noise field up to ± 8 Hz. Only in case of significant events or boisterous conditions, the sensor can sense pressure perturbations in the higher frequency range.

When the wind-noise levels are high, infrasound signals can be masked and remain undetected. Therefore, the sensor platform presents a passive anemometer to give insights into the wind conditions during infrasonic measurements. The MEMS anemometer is built up as an omnidirectional sensor. Numerical tests indicate that the temperature difference caused by a wind flow around the thermistors should be significant to be sensed. For validation, the anemometer has been calibrated inside a wind tunnel. Figure

~~3~~ 6 shows the outcome of the calibration tests. Based on this outcome, one can conclude that the anemometer can determine wind direction and wind speed, given that the sensor is calibrated. The sensor measures a difference in resistance, which is ~~relative compared to~~ converted into a temperature measurement. The discreet temperature measurements are used to reconstruct a 2D planar temperature gradient, which is used to determine the wind speed and direction. ~~Although the sensor is resolving wind direction and speed, the resolution is poor compared to the reference sensors. For the estimation of a~~ Based on the calibration tests within the windtunnel, it is shown that the anemometer has a directional accuracy of $\pm 5°$, and a wind speed accuracy of ± 2m/s. Nonetheless, it is shown in Figure 6-c that the anemometer has geometrical uncertainties, due to it design. Future anemometers, 2D ~~gradient (assuming the gradient is uniform), in principle only four degrees of freedom are needed: 2 in the x-direction, 2 in the y-direction. Therefore, the proposed system should be over determined in this case. Nonetheless, the resolution outcome of the MEMS anemometer shows opposite. It is likely that the temperature gradient is not strong enough to provide a wind direction resolution higher as 30°. A slight deviation is z position (a height difference) between the thermistors can cause such a reduction of temperature gradient~~hot-wire, should consider a minimum of 8 thermistors to exclude geometric uncertainties [Szuberla and Olson, 2004].

Besides an anemometer and infrasound sensor, the platform also hosts a barometric pressure sensor, an accelerometer, and GPS. Each sensor has been calibrated and compared with a reference sensor. It was shown that the accelerometer has a relatively high self-noise, which restricts the sensors ability to determine the ambient seismic noise ~~[Peterson, 1993] [McNamara and Buland, 2004]~~[Peterson, 1993, McNamara and Buland, 2004]. Nonetheless, the sensor will most likely resolve local transient events, which influences the ~~sensitivity of the~~ mini-MB's sensitivity and its ability to resolve infrasonic sources. The barometric sensor shows good agreement with a reference sensor (Figure ~~??~~5). Absolute pressure perturbations due to the weather are resolved. After calibration, the sensor has a precision of ± 0.1 hPa for 93% of the time. For the remainder maximum deviation, compared to the reference sensor, was ± 0.15 hPa.

Calibration tests, performed in this study and previous literature, show that the MEMS sensors perform less than the commonly used high-fidelity sensors. The self-noise of the sensors is a critical problem. Furthermore, the ~~manufacturer of the MEMS sensors highlight there is~~ MEMS sensors manufacturers highlight a significant change of measurement drift ~~[DLVR, 2019] [TDK, 2018] [STMicroelectronics, 2017] [STMicroelectronics, 2018]~~ [DLVR, 2019, TDK, 2018, STMicroelectronics, 2017, STMicroelectronics, 2018], regular calibration is needed. Nonetheless, the MEMS sensor techniques are continuously developing ~~[Jacob et al., 2014] [Johari, 2003]. The design of the "infrasound-logger"~~ [Jacob et al., 2014, Johari, 2003]. The INFRA-EAR design is such that the platform can be ~~adjust~~ adjusted and improved by adding or swapping sensors. Mobile sensor platforms, build up by PCB's and digital MEMS sensors, are therefor scalable, flexible, and ready for various geophysical measurements.

Nonetheless, a low-cost mobile multidisciplinary sensor platform can complement existing high-fidelity geophysical sensor networks. This study showed that, as long as the MEMS are well-calibrated, they perform in agreement with the reference sensors. Therefore, the ~~'infrasound-logger'~~ INFRA-EAR can contribute significantly to providing observations during ~~rapid deployments,~~ remote or rapid deployments (e.g., weather towers, weather balloons, and scientific balloons), to complement the existing sensor network by increasing ~~the number of~~ observations. Although the sensor data does not fully satisfy the measurement requirements, the ~~improve~~ improvement of spatial resolution enables stacking the observations. This can be realized by stacking the output of various sensor platforms ~~, or by~~ or adding more sensors to the same sensor platform and averaging the output [Nishimura et al., 2019]. Stacking improves the signal-to-noise ratio ~~increases~~ by $1/\sqrt{N}$, where N is the number of observations. ~~Furthermore, the platform enables measurement campaigns at remote places (e. g. , weather towers, weather balloons)~~

Initially, the INFRA-EAR has been designed as a biologger for the monitoring of atmospheric parameters. In total 25 INFRA-EAR's are produced and used during the 2020 field campaign at Crozet Island in the Southern Ocean. The loggers have been fitted to the Southern Ocean's largest seabirds, the Wandering Albatross (*Diomedea exulans*). The Southern Hemisphere has very little in situ measurements, due to limited shore areas. The use of INFRA-EAR in such areas is ideal for monitoring geophysical parameters, comparing in situ measurements, and comparing INFRA-EAR data with model data.

Acknowledgements

References

[Albarbar et al., 2009] Albarbar, A., Badri, A., Sinha, J. K., and Starr, A. (2009). Performance evaluation of mems accelerometers. *Measurement*, 42(5):790–795.

[Anderson et al., 2018] Anderson, J. F., Johnson, J. B., Bowman, D. C., and Ronan, T. J. (2018). The gem infrasound logger and custom-built instrumentation. *Seismological Research Letters*, 89(1):153–164.

[ANSYS,] ANSYS. Ansys academic research mechanical, release 18.1.

[Anthony et al., 2019] Anthony, R. E., Ringler, A. T., Wilson, D. C., and Wolin, E. (2019). Do low-cost seismographs perform well enough for your network? an overview of laboratory tests and field observations of the osop raspberry shake 4d. *Seismological Research Letters*, 90(1):219–228.

[Assink et al., 2018] Assink, J., Averbuch, G., Shani-Kadmiel, S., Smets, P., and Evers, L. (2018). A seismo-acoustic analysis of the 2017 north korean nuclear test. *Seismological Research Letters*, 89(6):2025–2033.

[Averbuch et al., 2020] Averbuch, G., Assink, J. D., and Evers, L. G. (2020). Long-range atmospheric infra-sound propagation from subsurface sources. *The Journal of the Acoustical Society of America*, 147(2):1264–1274.

[Blanc et al., 2018] Blanc, E., Ceranna, L., Hauchecorne, A., Charlton-Perez, A., Marchetti, E., Evers, L. G., Kvaerna, T., Lastovicka, J., Eliasson, L., Crosby, N. B., et al. (2018). Toward an improved representation of middle atmospheric dynamics thanks to the arise project. *Surveys in geophysics*, 39(2):171–225.

[Bowman and Lees, 2015] Bowman, D. C. and Lees, J. M. (2015). Infrasound in the middle stratosphere measured with a free-flying acoustic array. *Geophysical Research Letters*, 42(22):10–010.

[Brown et al., 2014] Brown, D., Ceranna, L., Prior, M., Mialle, P., and Le Bras, R. J. (2014). The idc seismic, hydroacoustic and infrasound global low and high noise models. *Pure and Applied Geophysics*, 171(3-5):361–375.

[Burridge, 1971] Burridge, R. (1971). The acoustics of pipe arrays. *Geophysical Journal International*, 26(1-4):53–69.

[Campus and Christie, 2010] Campus, P. and Christie, D. (2010). Worldwide observations of infrasonic waves. In *Infrasound monitoring for atmospheric studies*, pages 185–234. Springer.

[Christie and Campus, 2010] Christie, D. and Campus, P. (2010). The ims infrasound network: Design and establishment of infrasound stations. In *Infrasound monitoring for atmospheric studies*, pages 29–75. Springer.

[Cornes et al., 2020] Cornes, R. C., Dirksen, M., and Sluiter, R. (2020). Correcting citizen-science air temperature measurements across the netherlands for short wave radiation bias. *Meteorological Applications*, 27(1):e1814.

[676] [D'Alessandro et al., 2014] D'Alessandro, A., Luzio, D., and D'Anna, G. (2014). Urban mems based seismic
[677] network for post-earthquakes rapid disaster assessment. *Advances in Geosciences*.

[678] [De Bree et al., 2003] De Bree, H.-E. et al. (2003). The microflown: An acoustic particle velocity sensor.
[679] *Acoustics Australia*, 31(3):91–94.

[680] [DLVR, 2019] DLVR (2019). Technical Report DLVR Series Low Voltage Digital Pressure Sensors. `https:`
[681] `//www.allsensors.com/datasheets/DS-0300_Rev_E.pdf`.

[682] [Evers, 2008] Evers, L. G. (2008). *The inaudible symphony: on the detection and source identification of*
[683] *atmospheric infrasound.* PhD thesis, TU Delft, Delft University of Technology.

[684] [Evers and Haak, 2000] Evers, L. G. and Haak, H. W. (2000). *The Deelen Infrasound Array: on the detection*
[685] *and identification of infrasound.* Koninklijk Nederlands Meteorologisch Instituut.

[686] [Fang et al., 2010] Fang, Z., Zhao, Z., Du, L., Zhang, J., Pang, C., and Geng, D. (2010). A new portable micro
[687] weather station. In *2010 IEEE 5th International Conference on Nano/Micro Engineered and Molecular*
[688] *Systems*, pages 379–382. IEEE.

[689] [Formlabs, 2020] Formlabs (2020). *Technical Report Formlabs 3D printer.* Formlabs.

[690] [Garcia-Marti et al., 2019] Garcia-Marti, I., de Haij, M., Noteboom, J. W., van der Schrier, G., and de Valk,
[691] C. (2019). Using volunteered weather observations to explore urban and regional weather patterns in the
[692] netherlands. *AGUFM*, 2019:IN22A–08.

[693] [Gore-Tex, 2020] Gore-Tex (2020). *Technical Report Gore TEX air vents.* Gore-Tex.

[694] [Grangeon and Lesage, 2019] Grangeon, J. and Lesage, P. (2019). A robust, low-cost and well-calibrated
[695] infrasound sensor for volcano monitoring. *Journal of Volcanology and Geothermal Research*, 387:106668.

[696] [Green et al., 2012] Green, D., Matoza, R., Vergoz, J., and Le Pichon, A. (2012). Infrasonic propagation
[697] from the 2010 eyjafjallajökull eruption: Investigating the influence of stratospheric solar tides. *Journal of*
[698] *Geophysical Research: Atmospheres*, 117(D21).

[699] [Grimmett et al., 2019] Grimmett, D., Plate, R., and Goad, J. (2019). Measuring infrasound from the mar-
[700] itime environment. In *Infrasound Monitoring for Atmospheric Studies*, pages 173–206. Springer.

[701] [Haak and De Wilde, 1996] Haak, H. W. and De Wilde, G. (1996). *Microbarograph systems for the infrasonic*
[702] *detection of nuclear explosions.* Royal Netherlands Meteorological Institute, Seismology Division.

[703] [Homeijer et al., 2011] Homeijer, B., Lazaroff, D., Milligan, D., Alley, R., Wu, J., Szepesi, M., Bicknell, B.,
[704] Zhang, Z., Walmsley, R., and Hartwell, P. (2011). Hewlett packard's seismic grade mems accelerometer.
[705] In *2011 IEEE 24th International Conference on Micro Electro Mechanical Systems*, pages 585–588. IEEE.

[706] [Homeijer et al., 2014] Homeijer, B. D., Milligan, D. J., and Hutt, C. R. (2014). A brief test of the hewlett-
[707] packard mems seismic accelerometer. *US Geological Survey Open-file Report*, (2014-1047).

[708] [Hons et al., 2008] Hons, M., Stewart, R., Lawton, D., Bertram, M., and Hauer, G. (2008). Field data
[709] comparisons of mems accelerometers and analog geophones. *The Leading Edge*, 27(7):896–903.

[710] [Huang et al., 2003] Huang, Q.-A., Qin, M., Zhang, Z., Zhou, M., Gu, L., Zhu, H., Hu, D., Hu, Z., Xu, G.,
[711] and Liu, Z. (2003). Weather station on a chip. In *SENSORS, 2003 IEEE*, volume 2, pages 1106–1113.
[712] IEEE.

[713] [Jacob et al., 2014] Jacob, R. T., Manjiyani, Z. A. A., et al. (2014). Development of mems based 3-axis
[714] accelerometer for hand movement monitoring. *International Journal of Computer Science and Engineering*
[715] *Communications*, 2(1):87–92.

[716] [Johari, 2003] Johari, H. (2003). Development of mems sensors for measurements of pressure, relative hu-
[717] midity, and temperature.

[KNMI, 1993] KNMI (1993). Netherlands Seismic and Acoustic Network. Royal Netherlands Meteorological Institute (KNMI), Other/Seismic Network. 10.21944/e970fd34-23b9-3411-b366-e4f72877d2c5.

[Krishnamoorthy et al., 2020] Krishnamoorthy, S., Bowman, D. C., Komjathy, A., Pauken, M. T., and Cutts, J. A. (2020). Origin and mitigation of wind noise on balloon-borne infrasound microbarometers. *The Journal of the Acoustical Society of America*, 148(4):2361–2370.

[Laine and Mougenot, 2007] Laine, J. and Mougenot, D. (2007). Benefits of mems based seismic accelerometers for oil exploration. In *TRANSDUCERS 2007-2007 International Solid-State Sensors, Actuators and Microsystems Conference*, pages 1473–1477. IEEE.

[Lammel, 2015] Lammel, G. (2015). The future of mems sensors in our connected world. In *2015 28th IEEE International Conference on Micro Electro Mechanical Systems (MEMS)*, pages 61–64. IEEE.

[Ma et al., 2011] Ma, R.-H., Wang, Y.-H., and Lee, C.-Y. (2011). Wireless remote weather monitoring system based on mems technologies. *Sensors*, 11(3):2715–2727.

[Manobianco and Short, 2001] Manobianco, J. and Short, D. A. (2001). On the utility of airborne mems for improving meteorological analysis and forecasting. In *Conference on Modeling and Simulation of Microsystems*, pages 342–345.

[Marcillo et al., 2012] Marcillo, O., Johnson, J. B., and Hart, D. (2012). Implementation, characterization, and evaluation of an inexpensive low-power low-noise infrasound sensor based on a micromachined differential pressure transducer and a mechanical filter. *Journal of Atmospheric and Oceanic Technology*, 29(9):1275–1284.

[Marty, 2019] Marty, J. (2019). The ims infrasound network: current status and technological developments. In *Infrasound Monitoring for Atmospheric Studies*, pages 3–62. Springer.

[McNamara and Buland, 2004] McNamara, D. E. and Buland, R. P. (2004). Ambient noise levels in the continental united states. *Bulletin of the seismological society of America*, 94(4):1517–1527.

[Mentink and Evers, 2011] Mentink, J. H. and Evers, L. G. (2011). Frequency response and design parameters for differential microbarometers. *The Journal of the Acoustical Society of America*, 130(1):33–41.

[Merchant, 2015] Merchant, B. J. (2015). Hyperion 5113/gp infrasound sensor evaluation. *Sandia Report SAND2015–7075, Sandia National Laboratories*.

[Merchant and Hart, 2011] Merchant, B. J. and Hart, D. M. (2011). Component evaluation testing and analysis algorithms. *Sandia National Laboratories Technical Report No. SAND2011-8265*.

[Milligan et al., 2011] Milligan, D. J., Homeijer, B. D., and Walmsley, R. G. (2011). An ultra-low noise mems accelerometer for seismic imaging. In *SENSORS, 2011 IEEE*, pages 1281–1284. IEEE.

[Nief et al., 2017] Nief, G., Olivier, N., Olivier, S., and Hue, A. (2017). New optical microbarometer. In *AGU Fall Meeting Abstracts*, volume 2017, pages A21A–2150.

[Nief et al., 2019] Nief, G., Talmadge, C., Rothman, J., and Gabrielson, T. (2019). New generations of infrasound sensors: technological developments and calibration. In *Infrasound Monitoring for Atmospheric Studies*, pages 63–89. Springer.

[Nishimura et al., 2019] Nishimura, R., Cui, Z., and Suzuki, Y. (2019). Portable infrasound monitoring device with multiple mems pressure sensors. In *International Congress on Acoustics (ICA)*, pages 1498–1505.

[Peterson, 1993] Peterson, J. R. (1993). Observations and modeling of seismic background noise. Technical report, US Geological Survey.

[Poler et al., 2020] Poler, G., Garcia, R. F., Bowman, D. C., and Martire, L. (2020). Infrasound and gravity waves over the andes observed by a pressure sensor on board a stratospheric balloon. *Journal of Geophysical Research: Atmospheres*, 125(6):e2019JD031565.

[Ponceau and Bosca, 2010] Ponceau, D. and Bosca, L. (2010). Low-noise broadband microbarometers. In *Infrasound monitoring for atmospheric studies*, pages 119–140. Springer.

[Raspet et al., 2019] Raspet, R., Abbott, J.-P., Webster, J., Yu, J., Talmadge, C., Alberts II, K., Collier, S., and Noble, J. (2019). New systems for wind noise reduction for infrasonic measurements. In *Infrasound Monitoring for Atmospheric Studies*, pages 91–124. Springer.

[Raspet et al., 2008] Raspet, R., Yu, J., and Webster, J. (2008). Low frequency wind noise contributions in measurement microphones. *The Journal of the Acoustical Society of America*, 123(3):1260–1269.

[RBOOM, 2017] RBOOM (2017). Specifications for: Raspberry Boom (RBOOM) and 'Shake and Boom' (RSBOOM). https://manual.raspberryshake.org/_downloads/SpecificationsforBoom_SnB.pdf.

[Richiardone, 1993] Richiardone, R. (1993). The transfer function of a differential microbarometer. *Journal of Atmospheric and Oceanic Technology*, 10(4):624–628.

[Shani-Kadmiel et al., 2018] Shani-Kadmiel, S., Assink, J. D., Smets, P. S., and Evers, L. G. (2018). Seismoacoustic coupled signals from earthquakes in central italy: Epicentral and secondary sources of infrasound. *Geophysical Research Letters*, 45(1):427–435.

[Slad and Merchant, 2016] Slad, G. W. and Merchant, B. J. (2016). Chaparral model 60 infrasound sensor evaluation. *Technical Report*, pages SAND2016–1902.

[Sleeman et al., 2006] Sleeman, R., Van Wettum, A., and Trampert, J. (2006). Three-channel correlation analysis: A new technique to measure instrumental noise of digitizers and seismic sensors. *Bulletin of the Seismological Society of America*, 96(1):258–271.

[Smink et al., 2019] Smink, M. M., Assink, J. D., Bosveld, F. C., Smets, P. S., and Evers, L. G. (2019). A three-dimensional array for the study of infrasound propagation through the atmospheric boundary layer. *Journal of Geophysical Research: Atmospheres*, 124(16):9299–9313.

[Speller and Yu, 2004] Speller, K. E. and Yu, D. (2004). A low-noise mems accelerometer for unattended ground sensor applications. In *Unattended/Unmanned Ground, Ocean, and Air Sensor Technologies and Applications VI*, volume 5417, pages 63–72. International Society for Optics and Photonics.

[Steinhart and Hart, 1968] Steinhart, J. S. and Hart, S. R. (1968). Calibration curves for thermistors. In *Deep Sea Research and Oceanographic Abstracts*, volume 15, pages 497–503. Elsevier.

[STMicroelectronics, 2017] STMicroelectronics (2017). *Technical Report STMicroelectronics LPS33HW*. STMicroelectronics.

[STMicroelectronics, 2018] STMicroelectronics (2018). *Technical Report STMicroelectronics LSM303*. STMicroelectronics.

[Sutherland and Bass, 2004] Sutherland, L. C. and Bass, H. E. (2004). Atmospheric absorption in the atmosphere up to 160 km. *The Journal of the Acoustical Society of America*, 115(3):1012–1032.

[Szuberla and Olson, 2004] Szuberla, C. A. and Olson, J. V. (2004). Uncertainties associated with parameter estimation in atmospheric infrasound arrays. *The Journal of the Acoustical Society of America*, 115(1):253–258.

[TDK, 2018] TDK (2018). *Technical Report TDK NTC element G1540*. TDK.

[Texim Europe, 2013] Texim Europe (2013). *Technical Report Texim Europe GNS2301*. Texim Europe.

[Walker and Hedlin, 2010] Walker, K. T. and Hedlin, M. A. (2010). A review of wind-noise reduction methodologies. In *Infrasound monitoring for atmospheric studies*, pages 141–182. Springer.

[Washburn, 1921] Washburn, E. W. (1921). The dynamics of capillary flow. *Physical review*, 17(3):273.

[Waxler and Assink, 2019] Waxler, R. and Assink, J. (2019). Propagation modeling through realistic atmosphere and benchmarking. In *Infrasound Monitoring for Atmospheric Studies*, pages 509–549. Springer.

[Wessel et al., 2013] Wessel, P., Smith, W. H., Scharroo, R., Luis, J., and Wobbe, F. (2013). Generic mapping tools: improved version released. *Eos, Transactions American Geophysical Union*, 94(45):409–410.

[Wyngaard and Kosovic, 1994] Wyngaard, J. and Kosovic, B. (1994). Similarity of structure-function parameters in the stably stratified boundary layer. *Boundary-Layer Meteorology*, 71(3):277–296.

[Zirpel et al., 1978] Zirpel, M., Kraan, W., and Mastboom, P.-P. (1978). *Operationele versterkers: een verzameling schakelingen en formules voor de toepassing van operationele versterkers*. Kluwer.

[Zou et al., 2014] Zou, X., Thiruvenkatanathan, P., and Seshia, A. A. (2014). A seismic-grade resonant mems accelerometer. *Journal of Microelectromechanical Systems*, 23(4):768–770.
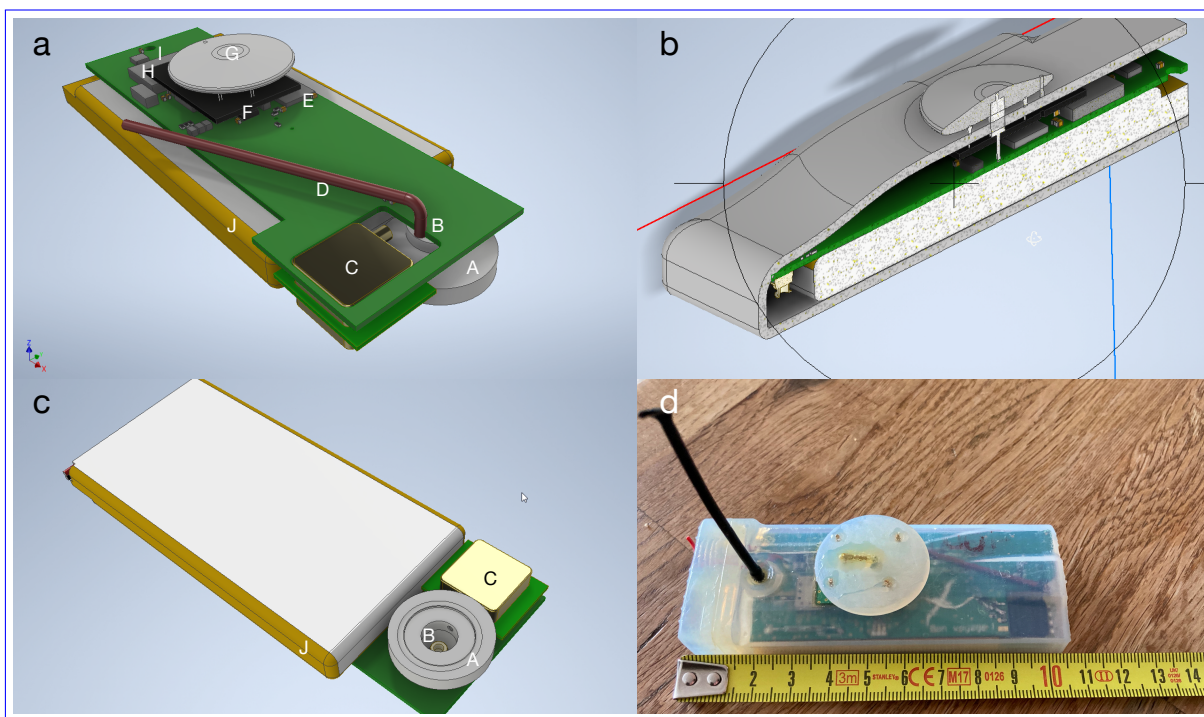
Figure 1: 3D CAD design of (a) the top of the PCB, (b) the casing, (c) the bottom of the PCB with pressure dome, and (d) a picture of the actual platform. The PCB hosts; a pressure dome (a-A/c-A), a barometric pressure sensor (a-B/c-B), a differential pressure sensor (a-C/c-C), a PEEKsil™ Red series capillary (a-D), an accelerometer (a-F), an anemometer (a-F) with ~~the~~ heating element (a-G), a ~~microcontroler~~ microcontroller (a-H), a GPS (a-I), and a lithium battery (a-J/c-J).
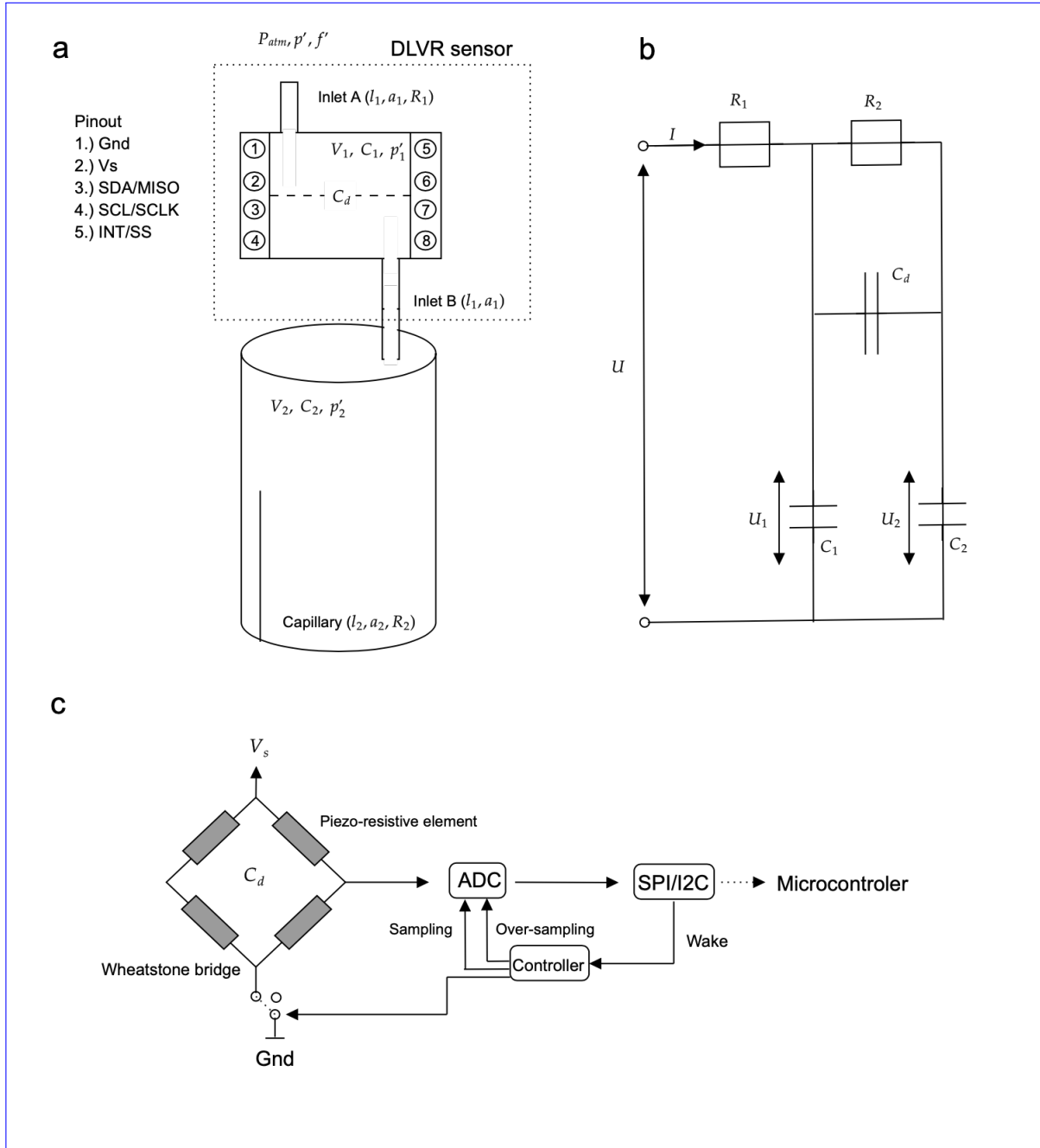
Figure 2: The KNMI mini-MB design with the DLVR sensor and the parameters as listed in Table 1 (a) ~~, as well as~~ and the electrical circuit of the mini-MB (b). Panel (c) visualises the DLVR sensor.
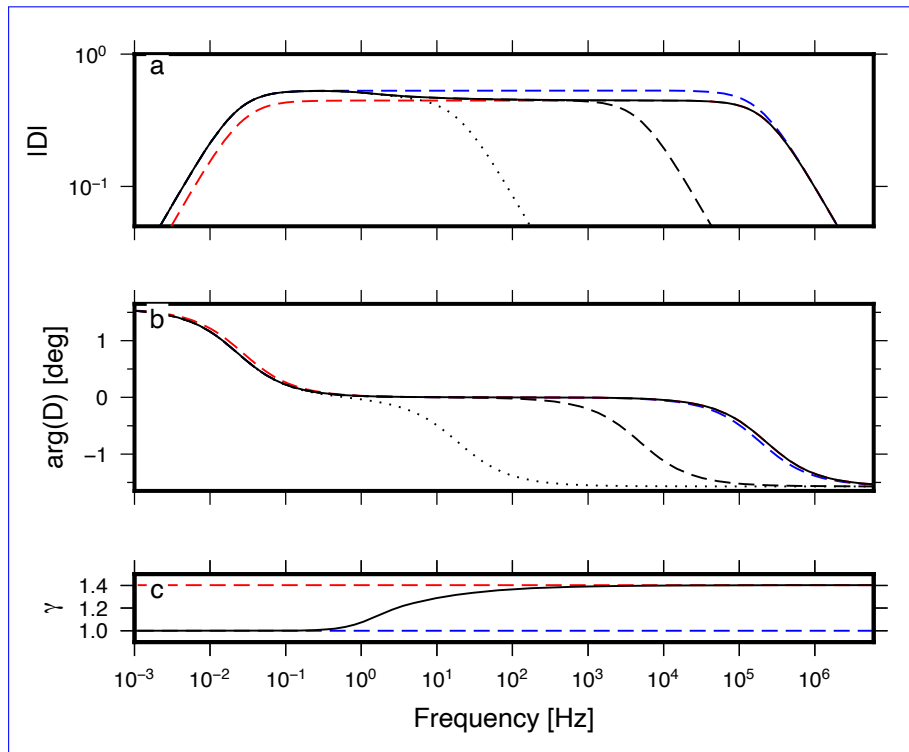
Figure 3: The theoretical sensor frequency response function for (a) amplitude and (b) phase in the case of isothermal and adiabatic gas behaviour in blue and red, respectively. The solid black line indicates the corrected sensor response by $\overline{\gamma}$ (c), as discussed in Section 3.1.3. The dotted and dashed line indicate the high-frequency shifting high frequency cut-off due to R_{gore}, as discussed in section 3.1.4.
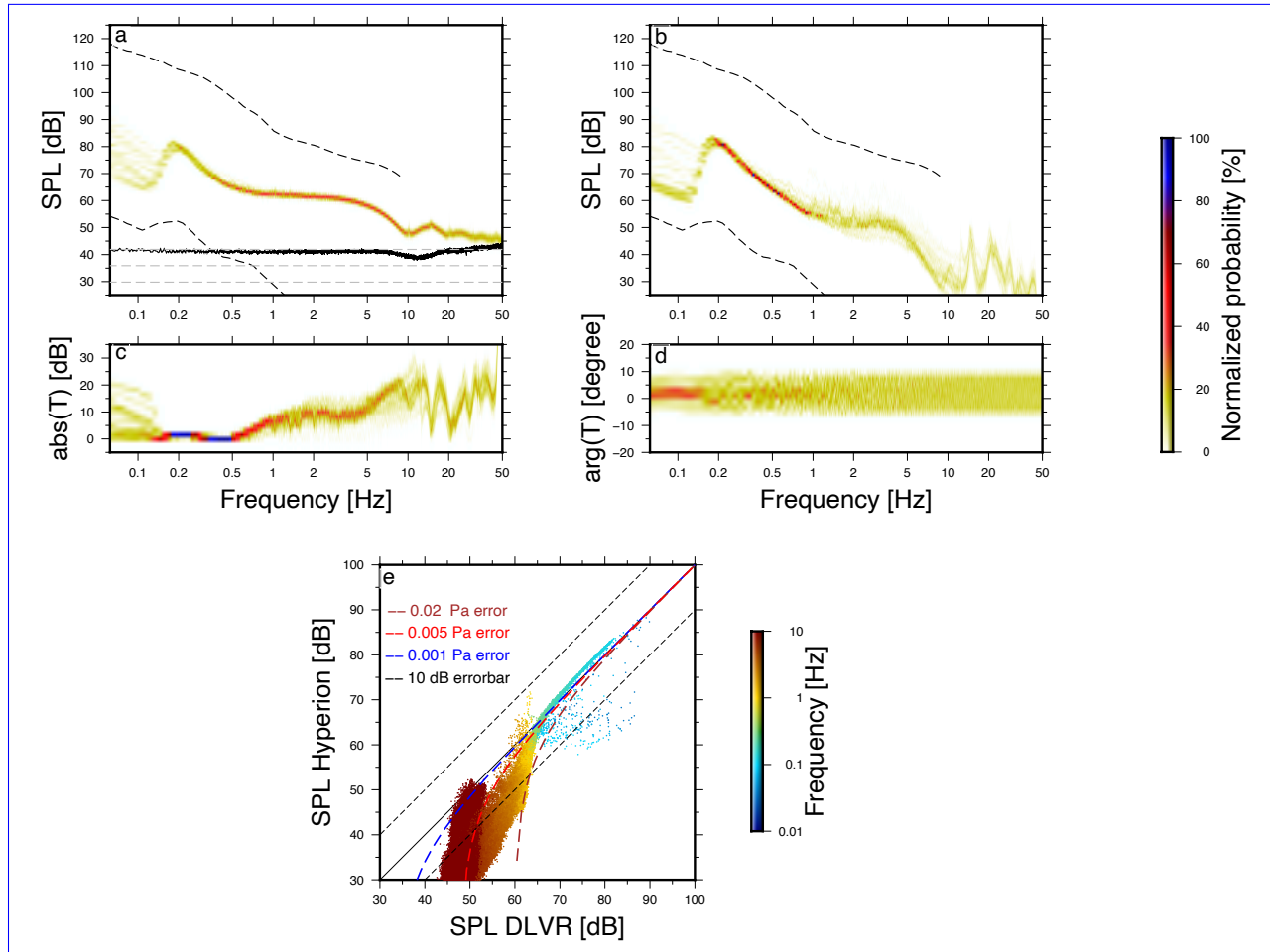
Figure 4: PDF's of pressure spectra recorded with the mini-MB (a) and the Hyperion sensor (b) for a week of continuous recording in dB re. 20^{-6} Pa^2/Hz. The ~~dotted~~ dashed lines indicate the infrasonic high and low ambient noise levels [Brown et al., 2014]. Panel (a) shows ~~as well~~ the PSD of the 24hr self-noise recording of the mini-MB in black, and the theoretical self-noise for a 12-, 13-, and 14-bit ADC as the gray dashed lines. Panels (c) and (d) visualise the absolute difference T in amplitude and phase between the mini-MB and the Hyperion as a function of frequency. Panel (e) displays the differences in sound pressure level measured by the mini-MB and the Hyperion sensor for the various frequencies.
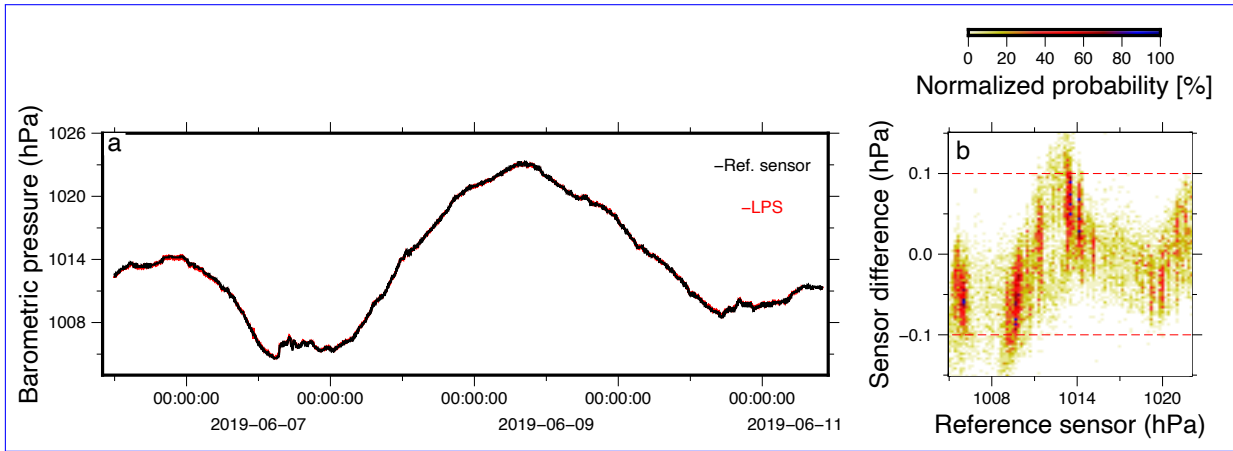
Figure 5: A comparison between the Barometric MEMS sensor (red) and a KNMI reference barometer (black). Panel (a) shows five days of barometric pressure recordings using both ~~sensor~~sensors, while panel (b) displays the difference in measured barometric pressure by the MEMS and the reference sensor.
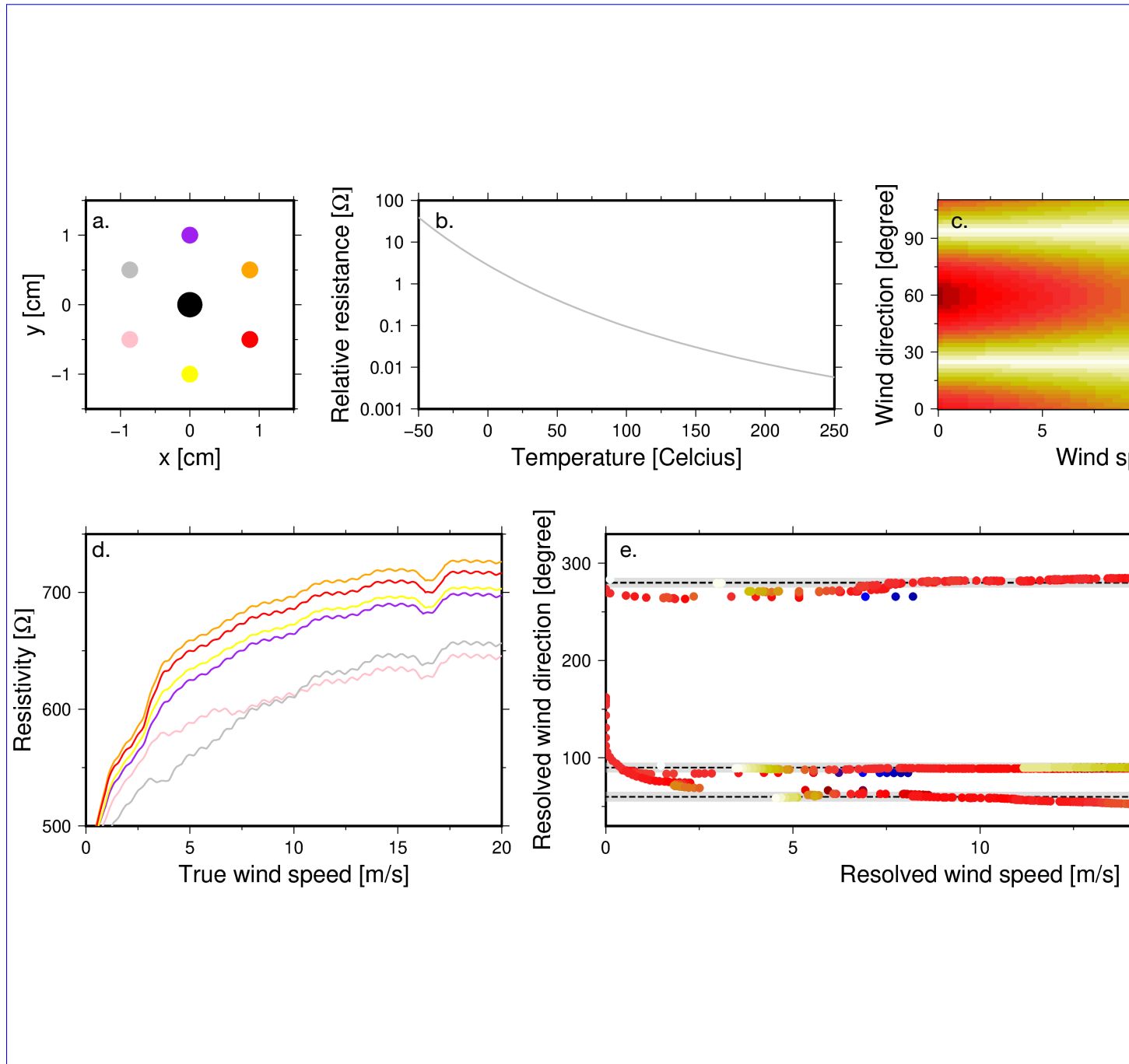
Figure 6: Analyses of the anemometer. Panel a shows the top view of the sensor design, with the central heating element. Panel b indicates the resistivity of the thermistors over temperature. The ~~measured resistance of~~ geometric sensitivity for the anemometer is shown in panel c. The thermistors' measured resistance for calibration set-up ~~a~~2 (90°), the colors are in agreement with the sensor design (a), are shown in panel ~~e~~d. ~~The solid black line is the average 4th order polynomial fit.~~ Panel ~~d~~ e indicates the resolved wind direction ~~(solid lines)~~ and wind speed compared with the ~~expected~~ actual direction (dotted lines) and correct wind speed of set-ups ~~a~~1 (270°), ~~b~~2 (90°), and ~~e~~3 (60°). The gray shaded area indicates the ±5° accuracy interval.
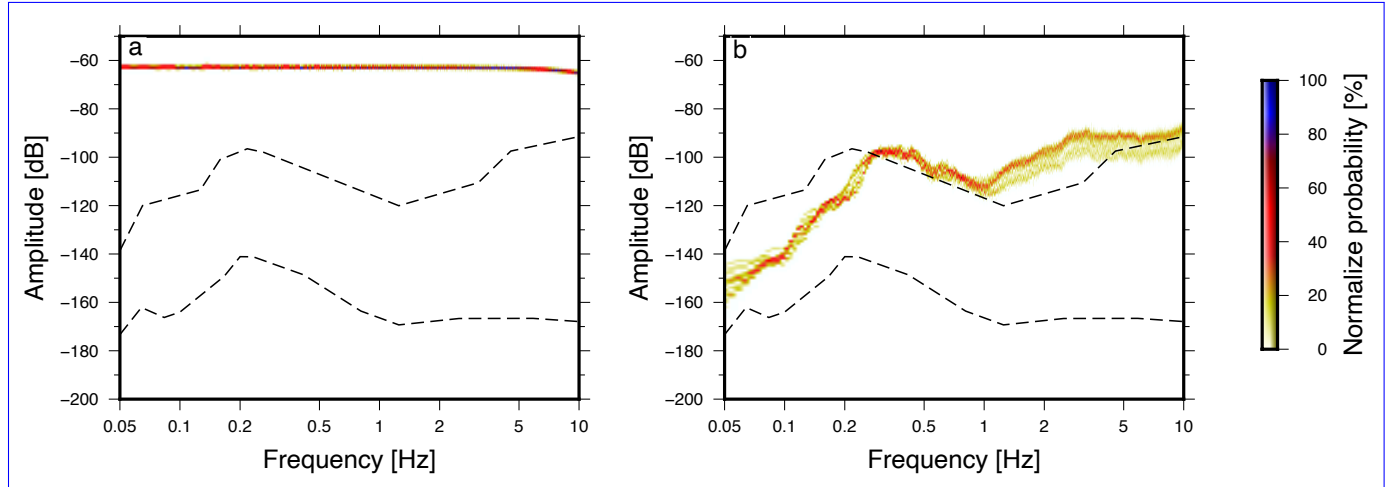
Figure 7: PDF's of the LSM IMU accelerometer (a) and the Streckeisen STS-2 connected to a Quanterra Q330 (b) for 24 hours of continuous recording in dB re. $m^2s^{-4}Hz^{-1}$. The dotted lines indicate the seismic high and low ambient noise levels [Peterson, 1993].